Self patterning induced by a solutal Marangoni effect in a receding drying meniscus

F. Doumenc[1] [(a)] and B. Guerrier[1]

[1] *UPMC Univ Paris 06, Univ Paris-Sud, CNRS, lab. FAST, bat 502, Campus Univ., Orsay F-91405, France*

PACS 40.47.54.-r Pattern selection; pattern formation
PACS 40.47.15gm Thin film flows
PACS 40.47.55.np Contact lines
PACS 40.47.57.Ng Polymers and polymer solutions

Abstract – This paper examines through numerical simulations the impact of a solutal Marangoni effect on the deposit obtained from a polymer solution. A hydrodynamical model with lubrication approximation is used to describe the liquid phase in a dip-coating-like configuration. The studied case considers evaporation in stagnant air (diffusion-limited evaporation), which results in a coupling between the liquid and gas phases. Viscosity, surface tension, and saturated vapor pressure depend on the solute concentration. In the evaporative regime, when the surface tension increases with the polymer concentration, the Marangoni effect induces a periodic regime. This results in a self-organized periodic patterning of the dried film in certain control parameter ranges. A morphological phase diagram as well as meniscus and dry deposit shapes are provided as a function of the substrate velocity and bulk solute concentration.

Introduction. – Recent years have seen important developments in studies dedicated to patterning induced by convective self-assembly during the drying of solutions or dispersions. For geometries such as sessile droplets or dip-coating-like configurations, the system may develop regular patterns induced by a periodic movement of the contact line. The contact line is pinned, or slows down compared to the mean velocity, and then speeds up (slip event) until the next pinning event [1, 2]. A remarkable aspect of this phenomenon is its universality: it can be observed for different geometries (sessile droplet [3], liquid bridge [4], capillary tube [5], dip-coating [6] or similar geometry [7,8]) and different solutes (colloids [9], polymers [10], small molecules [11], etc.).

Despite the large number of experimental and theoretical studies published in the last ten years, we are still lacking a complete understanding of the mechanisms responsible for the appearance of a periodic regime (see Frastia et al. [12] for a recent and complete review). A very promising approach, which motivated the present work, consists in capturing a stick-slip phenomenon through a hydrodynamical model. Such models were developed to describe the evaporation of dewetting liquid layers (Warner et al. [13], Frastia et al. [12,14]), of droplets (Craster et al [15]), or the transfer of a surfactant monolayer over a moving substrate (Köpf et al [16]). All of these models are based on lubrication approximation and concern thin liquid layers in a situation of partial wetting (substrate wettability is taken into account through a disjoining pressure term). Evaporation is assumed to be phase transition-limited (a situation that occurs when the liquid is in contact with its pure vapor); the dynamic in the gas phase can therefore be disregarded (one-sided models). With the exception of [16], these models consider colloidal dispersions, which are characterized by strong variations of viscosity as a function of particle concentration (Krieger-Dougherty law, which diverges at the maximum particle packing concentration). Additionally, Warner et al. [13] and Köpf et al. [16] have studied the solutal Marangoni effect's influence on the pattern formation (due to the presence of a surfactant, which lowers the liquid surface tension). An advantageous feature shared by all of these models is their ability to predict the periodic patterning of the deposit without an artificial trigger. For instance, the periodic movement of the contact line can be produced by alternate motions of dewetting and drying fronts that are competing against each

[(a)] E-mail: doumenc@fast.u-psud.fr

other [12,14].

In this study, we consider a polymer solution drying in stagnant air in a dip-coating-like geometry (a meniscus over a moving substrate). Because the substrate velocity is a control parameter, this set-up corresponds to an active geometry as defined in [12]. Our adopted approach is similar to the above-discussed models, although it includes specific features relevant to our studied problem. First, we consider that evaporation takes place in stagnant air (diffusion-limited evaporation), which requires us to take account of the diffusion dynamic in the gas phase. Secondly, surface tension is assumed to depend on the polymer concentration (solutal Marangoni effect). However, in contrast to the above-mentioned works, the non-volatile solute has a higher surface tension than the volatile solvent. Finally, we consider the saturated vapor pressure's dependence on the solvent concentration. The evaporation flux decreases with the solvent concentration, and the film thickness therefore remains large enough to maintain a negligible influence of substrate wettability, thus the disjoining pressure is disregarded in the model.

Previous results obtained for this same configuration have disregarded the Marangoni effect [17]. Although these previous simulations have confirmed the impact of local evaporation on the shape of the meniscus and predicted the deposit thickness, only flat deposits were observed. In this work, we demonstrate that the solutal Marangoni effect may be one of the mechanisms responsible for the onset of a periodic regime. Indeed, when the non-volatile solute has a higher surface tension than the solvent and for a certain range of substrate velocities and bulk concentrations, a stable steady solution does not exist, and the system spontaneously evolves toward a periodic solution.

The film/gas model. – This study examines a drying binary solution (one volatile solvent and one non-volatile solute) in a meniscus. The free surface is in contact with air at atmospheric pressure and evaporation is limited by the diffusion of solvent vapor into stagnant air. Our conditions assume a local thermodynamic equilibrium at the interface at a constant temperature (isothermal problem). The solution is in contact with a moving, flat substrate with a no-slip boundary condition. The model is two-dimensional, and the hydrodynamics inside the solution are described in a lubrication approximation framework. Gravity is neglected, and a uniform concentration over the thickness is assumed in the liquid phase.

The direction parallel to the substrate (flow main direction) is denoted by $\vec{x}$; the axis normal to the substrate is denoted by $\vec{z}$. With the above-mentioned approximations and assuming a Newtonian fluid, Stokes equations produce the following standard result [18]:

$$Q(x,t) = V_{sub}h + \frac{h^3}{3\eta(\phi)}\frac{\partial}{\partial x}(\gamma\frac{\partial^2 h}{\partial x^2}) + \frac{h^2}{2\eta(\phi)}\frac{\mathrm{d}\gamma}{\mathrm{d}\phi}\frac{\partial \phi}{\partial x}, \quad (1)$$

where V_{sub} is the substrate velocity, h is the liquid height, η is the dynamic viscosity, γ is the surface tension, and ϕ is the polymer volume fraction. $Q(x,t)$ is the liquid volumic flux (by unit of width) at abscissa x and time t over a cross-section normal to $\vec{x}$,

$$Q(x,t) = \int_0^{h(x)} u(x,z)\,\mathrm{d}z, \quad (2)$$

where $u(x,z)$ is the velocity component in the $\vec{x}$ direction. The first term on the right-hand side of eq. (1) is the flow produced by the substrate motion; the second term is the flow induced by capillary pressure; the last term describes the flow driven by the surface tension gradient (Marangoni effect). In the following, these three terms are denoted by Q_{sub}, Q_{cap}, and Q_{Ma}, respectively. The global mass conservation and the non-volatile solute mass conservation respectively read as follows:

$$\frac{\partial h}{\partial t} + \frac{\partial Q}{\partial x} = -v_{ev}(x,t) \quad (3)$$

$$\frac{\partial(\phi h)}{\partial t} + \frac{\partial(\phi Q)}{\partial x} = \frac{\partial}{\partial x}(Dh\frac{\partial \phi}{\partial x}), \quad (4)$$

where $v_{ev}(x,t)$ is the local evaporation velocity (positive for evaporation), and D is the mutual diffusion coefficient of the binary system.

At $x = 0$ (inlet of the computational domain) we impose the liquid height h_0, the curvature C_0, and the bulk solute volume fraction ϕ_0:

$$\text{at } x = 0,\ h = h_0,\ \frac{\partial^2 h}{\partial x^2} = C_0,\ \phi = \phi_0. \quad (5)$$

Considering, for instance, a capillary rise between two plates separated by a gap d, C_0 is the curvature of a static meniscus deduced from the gap d between the plates ($C_0 = 2/d$). The height h_0 is an arbitrary cut-off; it must be small enough to ensure the validity of a small slope approximation. Imposing h_0 and C_0 at $x = 0$ creates a meniscus section of static length $L_{st} \sim \sqrt{h_0/C_0}$. Variations of curvature and height at $x = 0$, produced by the evaporation or the substrate motion, are neglected in this approach.

For the outlet conditions at $x = W$, far away from the bulk, we assume a zero concentration gradient:

$$\text{at } x = W,\ \frac{\partial \phi}{\partial x} = 0. \quad (6)$$

In the evaporative regime (cf. next section) the film is dry at the outlet and we consider $\phi(W,t) \sim 1$, which results in a very large viscosity close to the outlet. We can therefore infer that eq. (1) reduces to $Q(x,t) \simeq V_{sub}h$ in that region, thus eq. (3) turns into an advection equation of order 1 in space, which does not require any boundary conditions at $x = W$. In the Landau-Levich regime we assume a zero slope and curvature at the outlet.

The local evaporation velocity $v_{ev}(x,t)$ in eq. (3) is determined by solving a diffusion problem in the gas phase

for a domain of length W and height H (H would roughly correspond to the boundary layer thickness for a process with a forced air-flow above the free surface). Because H is considerably larger than h_0, we assume a rectangular domain for the gas phase. The liquid thickness variations are therefore neglected in the computation of the mass transfer in the gas phase. The bottom boundary of this domain corresponding to the liquid-gas interface is thus: $z = 0$ and $0 < x < W$. The diffusion equation in the gas phase reads as follows:

$$\frac{\partial c_g}{\partial t} = D_g\left(\frac{\partial^2 c_g}{\partial x^2} + \frac{\partial^2 c_g}{\partial z^2}\right), \text{ for } 0 < x < W \text{ and } 0 < z < H\,, \tag{7}$$

where c_g is the solvent vapor concentration in the air, and D_g is the vapor diffusion coefficient. The vertical walls are assumed to be impermeable. A Dirichlet condition with a zero solvent vapor concentration is imposed at the top. We thus obtain the following boundary conditions for the gas domain (see fig. 1):

$$\frac{\partial c_g}{\partial x} = 0 \text{ for } (x = 0 \text{ or } x = W) \text{ and } 0 < z < H \tag{8}$$

$$c_g = 0 \text{ for } 0 \leq x \leq W \text{ and } z = H \tag{9}$$

The next boundary condition corresponds to the coupling between the liquid and the gas phases. The solvent activity in a polymer solution is given by the classical Flory-Huggins theory [19]: $a = (1-\phi)exp(\phi + \chi\phi^2)$, where χ is the polymer-solvent interaction parameter. Given the assumption that the vapor behaves as an ideal gas, the local thermodynamic equilibrium at the interface implies $a = P_{vs}/P_{vs0}$, where P_{vs} and P_{vs0} are the saturated vapor pressure above the solution and the pure solvent, respectively. The vapor solvent concentration at the interface can be deduced from the solvent activity and the ideal gas law:

$$c_g = a(\phi, T)P_{vs0}(T)\frac{M_s}{RT} \text{ for } 0 \leq x \leq W \text{ and } z = 0, \tag{10}$$

where M_s is the solvent molar mass, R is the ideal gas constant, and T is the temperature. Equation (10) neglects Kelvin effect. The validity of this assumptions has been confirmed a posteriori by inspection of the numerical results. Our final equation concerns the mass flux conservation across the interface:

$$\rho v_{ev} = -D_g\frac{\partial c_g}{\partial z}, \tag{11}$$

where ρ is the liquid solvent density. In agreement with [17], the above set of equations (1 to 11) is solved through finite differences (using a pure implicit scheme of order 1 in time and 2 in space and an adaptive spatial mesh to increase the density of nodes in the high concentration gradient region). Results of a previous calculus for a close configuration provided the initial conditions. In the following, we focus on the long term behavior, and the initial transient regimes are not shown.

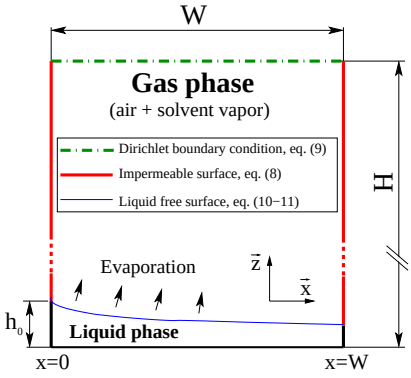

Fig. 1: Geometry and boundary conditions of the gas domain.

The solution provides the meniscus shape, the local evaporation flux, the concentration field in the gas, and the concentration and velocity fields in the solution (cf. [17] for details of a configuration without the Marangoni effect). The following values apply to all simulations: $H = 3\,\text{mm}$, $W = 1\,\text{mm}$, $C_0 = 2\,\text{mm}^{-1}$, $h_0 = 0.1\,\text{mm}$, and $T = 25^o\text{C}$ for the physico-chemical properties of the Polyisobutylene (PIB)/toluene system [17]. The toluene saturated vapor pressure, the molar mass and the diffusion coefficient in the gas phase are $P_{vs0} = 3792\,\text{Pa}$, $M_s = 92.14\,\text{g.mol}^{-1}$, and $D_g = 8.6 \times 10^{-6}\,\text{m}^2\text{.s}^{-1}$, respectively. The solution density and the diffusion coefficient are assumed to be constant: $\rho = 900\,\text{kg.m}^{-3}$ and $D = 10^{-10}\,\text{m}^2\text{.s}^{-1}$. The surface tension γ is assumed to increase linearly with the solute volume fraction from $\gamma = 28 \times 10^{-3}\,\text{N.m}^{-1}$ (pure toluene) to $\gamma = 34 \times 10^{-3}\,\text{N.m}^{-1}$ (pure PIB). The viscosity η exhibits a strong increase with the solute volume fraction (12 orders of magnitude from pure toluene to pure PIB for a PIB molar mass of $M_W = 500\,\text{kg.mol}^{-1}$). The following empirical law gives η in Pa.s: $Y = 8.22 + 13.2X + 5.2X^2 + 0.70X^3$, where $Y = log_{10}(\eta)$ and $X = log_{10}(\phi)$. Gravimetric experiments [20] have measured the PIB-toluene interaction parameter as follows: $\chi = 0.45 + 0.30\phi$ at $T = 25^o\text{C}$.

Results and discussion. – Fig.2 illustrates the solutions obtained for different substrate velocities at $\phi_0 = 0.01$. A steady regime is always observed for the reference configuration without the Marangoni effect ($\text{d}\gamma/\text{d}\phi = 0$, $\gamma = \gamma(\phi_0)$, black dashed curves). Previous studies have shown that evaporation at the meniscus significantly impacts the flow [17] for this range of substrate velocities ($10\,\mu\text{m.s}^{-1} \leq V_{sub} \leq 100\,\mu\text{m.s}^{-1}$). The deposit thickness h_d can be obtained through simple mass balances [11, 17, 21, 22]:

$$h_d = F_{ev}\phi_0/V_{sub}, \tag{12}$$

where F_{ev} is the integral of the evaporation velocity v_{ev} over the whole meniscus. The dry film thickness in this evaporative regime, where most of the evaporation takes place in the meniscus, corresponds to the left branch in fig.3. At higher substrate velocity, the right branch corre-

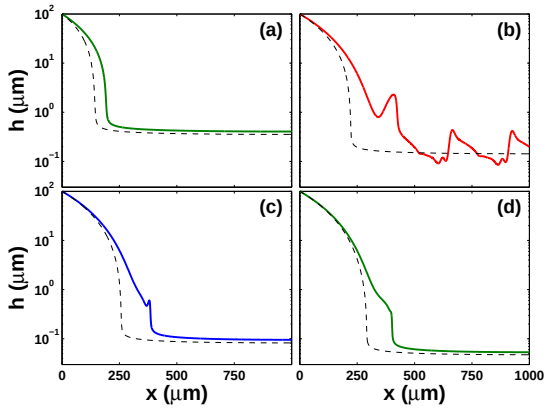

Fig. 2: Liquid height for different substrate velocities, $\phi_0 = 0.01$. Dashed lines: constant surface tension (no Marangoni effect). Solid lines: variable surface tension (Marangoni effect). (a)$V_{sub} = 10\mu$m/s (steady sub-regime, monotonic profile), (b)$V_{sub} = 30\mu$m/s (periodic sub-regime, moving bump), (c)$V_{sub} = 55\mu$m/s (steady sub-regime, stationary bump), (d)$V_{sub} = 100\mu$m/s (steady sub-regime, monotonic profile).

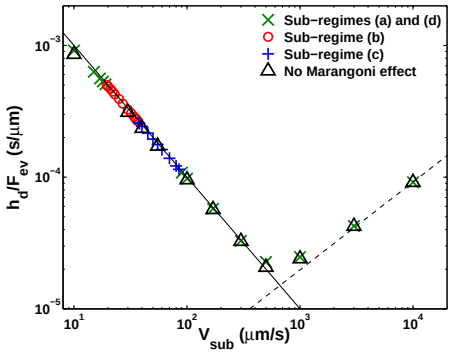

Fig. 3: Dry film thickness divided by evaporation flux for $\phi_0 = 0.01$. Solid line: eq. (12) (evaporative regime). Dashed line: slope 2/3 (Landau-Levich regime). For the sub-regime case (b) (red circles), the thickness is averaged over one period.

sponds to the Landau-Levich regime, where viscous forces drag a film onto the substrate; this film subsequently dries [11, 23]. The deposit thickness is proportional to $V_{sub}^{2/3}$ in this regime, as expected. When the Marangoni effect is considered, complex behaviors are observable in the evaporative regime. First, because the surface tension of the solute is higher than that of the solvent, the concentration gradient causes the meniscus to be stretched compared with the case without the Marangoni effect (solid lines v. dashed lines in fig.2). The formation of a stationary bump in the sub-regime (c), corresponding to the velocity range $37\,\mu$m.s$^{-1} < V_{sub} \leq 85\,\mu$m.s^{-1}, is a significant fact. The bump size decreases when V_{sub} increases, and a monotonic profile is recovered for $V_{sub} > 85\,\mu$m.s^{-1} (sub-regime (d)). Poulard and Damman [25] have experimentally observed such a bump, induced by a solutal Marangoni flow, during the drying of a polymer solution droplet. For a simpler case (pure liquid and a uniform surface tension gradient imposed by heating the substrate), Carles and Cazabat [24] have advanced an elegant discussion to explain the bump formation using simple hydrodynamical arguments based on mass conservation in a steady state (cf. [24] for details). Our study considers a more complex configuration because the meniscus shape is the result of a complex interplay between the three components of the volumic flux and the variable viscosity. However similar arguments can be put forward to qualitatively understand the origin of the stationary bump. Indeed, to ensure mass conservation in the steady state (eq. (3) with $\frac{\partial h}{\partial t} = 0$), the Marangoni flux Q_{Ma} must be balanced by a modification of the capillary flux Q_{cap}. This is illustrated in fig.4, which shows the three components (Q_{sub}, Q_{cap}, and Q_{Ma}) of the liquid volumic flux $Q(x)$. Q_{Ma} is always positive but non-monotonic. The capillary term changes its sign to ensure mass conservation, and so does the third derivative of the height $h(x)$, which results in the bump formation. Below a given substrate velocity ($V_{sub} \leq 37\,\mu$m.s^{-1} in our example), a stationary solution is no longer achievable and the numerical simulation converges toward a periodic solution, leading to a regularly patterned deposit (sub-regime (b) in fig.2). The time evolution of the liquid height profile is detailed over one period in fig.5, where the black arrow indicates the bump top. The dotted vertical line is the drying front corresponding to the limit of the "frozen" region, where the liquid viscosity is so large that the liquid film is simply advected at the substrate velocity. In practice, we consider the drying front to be located at the abscissa x_f defined by $(Q(x_f,t) - Q_{sub}(x_f,t))/Q_{sub}(x_f,t) < 1\%$. In this periodic regime, the bump initially grows upward while simultaneously moving to the right, preceded by the drying front; both of them move away from the meniscus. After a certain time, the drying front recedes, causing the bump to dry with a dramatic increase in viscosity. The bump is then advected at the substrate velocity, and a new bump is formed closer to the meniscus, and so on. Finally, for a lower substrate velocity ($V_{sub} < 19.5\,\mu$m.s^{-1} in our example), we again observe a steady regime with a monotonic liquid height profile (sub-regime (a) in fig.2).

It is noteworthy that, while the meniscus shape is strongly sensitive to the Marangoni effect, the dry deposit thicknesses (averaged over one period for the periodic regime case) are recovered without significant changes compared with the simulations without the Marangoni effect (cf. fig.3). It follows that the global mass balances are not affected by the development of the flow induced by the surface tension gradient.

Fig.6 depicts a morphological phase diagram of the different regimes as a function of V_{sub} and ϕ_0, illustrating that the periodic regime occurs in a relatively small range of substrate velocities and disappears for bulk concentrations larger than about 0.03.

Concerning the periodic sub-regime (b), fig.7 illustrates wavelengths and amplitudes of the periodic patterns as a

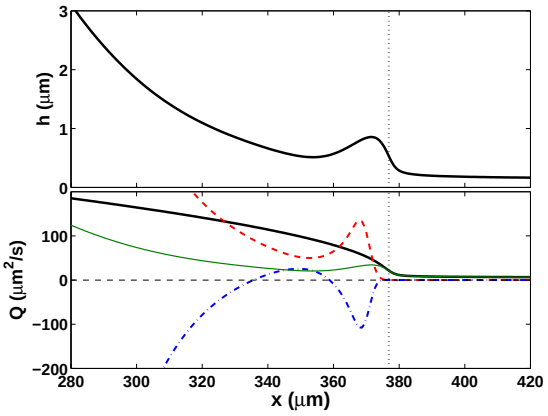

Fig. 4: Relation between meniscus profile and liquid fluxes for $V_{sub} = 40\mu m.s^{-1}$ and $\phi_0 = 0.01$ (steady state, zoom on the bump region). Top: liquid height. Bottom: total liquid volumic flux Q (thick black line), Q_{sub} (thin green line), Q_{cap} (dashed-dot blue line) and Q_{Ma} (dashed red line). Dotted vertical line: position of the drying front corresponding to the abscissa x_f, so that $(Q(x_f,t) - Q_{sub}(x_f,t))/Q_{sub}(x_f,t) < 1\%$.

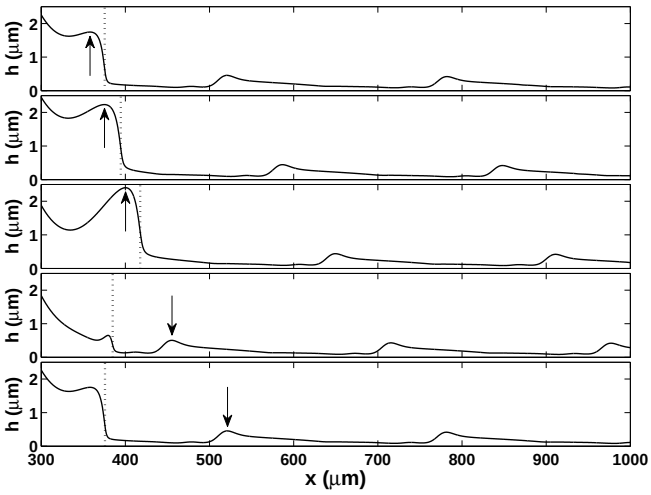

Fig. 5: Periodic time evolution of the meniscus (the region from $x = 0$ to $x = 300\,\mu$m is not shown). $V_{sub} = 30\,\mu\text{m.s}^{-1}$, $\phi_0 = 0.01$. From top to bottom: $t = 0$, $t = 0.25\tau$, $t = 0.5\tau$, $t = 0.75\tau$, $t = \tau$, where the period $\tau = 8.69s$. The black arrow indicates the bump top. The dotted vertical line is the position of the drying front corresponding to the abscissa x_f, so that $(Q(x_f,t) - Q_{sub}(x_f,t))/Q_{sub}(x_f,t) < 1\%$.

function of the substrate velocity and for two bulk concentrations. Note that these results correspond to the morphology of the film outside of the meniscus, where the system gels due to the very high viscosity of the solution. Therefore, in that region, the periodic pattern is simply translated at the substrate velocity V_{sub}. We use the period τ to obtain the wavelength $\lambda = \tau V_{sub}$; the pattern amplitude refers to the dry deposit thickness $h_d = h\phi$. Qualitatively, fig.7 shows two types of transitions from flat to patterned deposit: (α) at low velocity, a divergence of the wavelength for a finite value of V_{sub} occurs whereas the amplitude retains a quasi-constant value; (β) at high velocity, a decrease of the pattern amplitude is observed. For both cases, small domains of hysteresis are observed close to the transition regions. Indeed the substrate velocity corresponding to the transition from a flat to a patterned deposit can be slightly shifted (less than 1μm/s) by changing the initial condition (flat deposit limits shown in fig.7 correspond to a decreasing substrate velocity). Li et al. [26] have also observed a divergence of the wavelength when the substrate velocity was decreased (numerical simulations of Langmuir-Blodgett transfer), and it is worth noting that behaviors (α) and (β) have already been reported by Frastia et al [12], although their study was based on a different situation (numerical simulations of a dewetting thin film with a passive geometry). As suggested by these authors, one may infer that, most likely, behavior (α) corresponds to a homoclinic bifurcation and behavior (β) corresponds to a subcritical Hopf bifurcation. A more precise description would require the definition of a reduced model and a subsequent analysis within the framework of bifurcation theory; this was performed, for instance, by Köpf et al. [27] for Langmuir-Blodgett transfer.

Fig.8 illustrates the complex behavior of the system for a step-by-step decrease of V_{sub} at $\phi_0 = 0.01$. Starting from a steady state ($V_{sub} = 38\,\mu$m/s, flat deposit), we obtain periodic regimes at $V_{sub} = 37, 36.5$ and $36\,\mu$m/s (fig.8-(1-3)), with a doubling of the wavelength between the last two velocities. After passing through an aperiodic regime ($V_{sub} = 35.75\mu$m/s, fig.8-4), a new periodic regime is reached, characterized by a larger wavelength and a significant change in the amplitude and deposit shape ($V_{sub} = 35.5\,\mu$m/s, fig.8-5). Fig.8-(1-3) and fig.8-5 correspond to the fourth righthandmost circles in fig.7. The aperiodic regime observed in fig.8-4 is not represented in fig.7 (undefined wavelength).

The decrease of the pattern amplitude with an increasing substrate velocity has already been experimentally observed [7]. However, in these experiments, which were performed with colloidal suspensions, the wavelengths have remained proportional to V_{sub}^{-1} for over a decade, suggesting that mechanisms other than the solutal Marangoni effect may be involved and should therefore be investigated. The study of two dimensional patterns offers another interesting perspective. Indeed, it is well known that the liquid bump observed in these simulations is subject to the Rayleigh-Plateau instability [25, 28], which has the potential to produce a rich variety of different patterns.

* * *

This work received support from the EU through the ITN MULTIFLOW (PITN-GA-2008-214919).

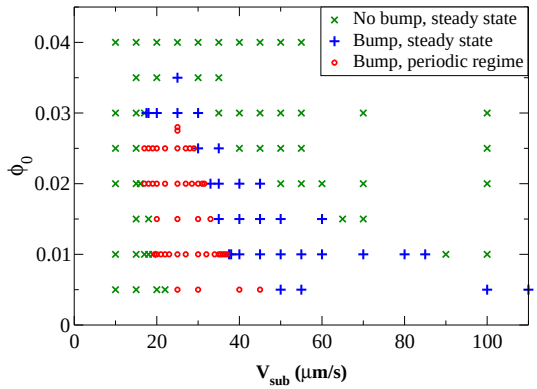

Fig. 6: Morphological phase diagram of meniscus shape, in the plane spanned by the substrate velocity V_{sub} and the bulk polymer volume fraction ϕ_0.

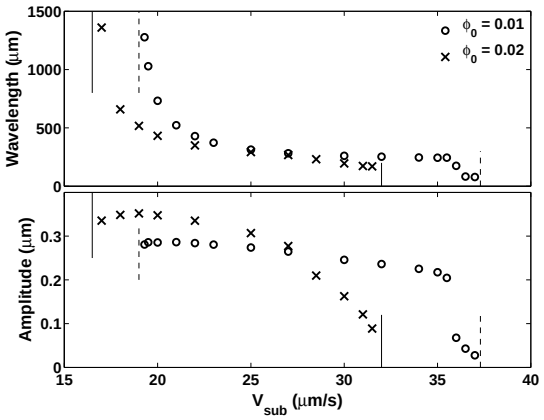

Fig. 7: Pattern wavelength (top) and amplitude (bottom) in the periodic sub-regime. Dashed vertical lines: flat deposit for $\phi_0 = 0.01$. Solid vertical lines: flat deposit for $\phi_0 = 0.02$.

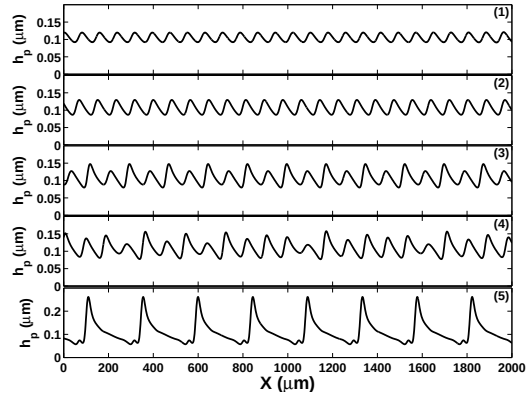

Fig. 8: Transition from flat to patterned deposit for $\phi = 0.01$ and decreasing substrate velocity, starting from steady state at $V_{sub} = 38\mu$m/s (flat deposit, not shown). (1) $V_{sub} = 37\mu$m/s, $\lambda = 78.4\mu$m ; (2) $V_{sub} = 36.5\mu$m/s, $\lambda = 82.1\mu$m ; (3) $V_{sub} = 36\mu$m/s, $\lambda = 175\mu$m ; (4) $V_{sub} = 35.75\mu$m/s, aperiodic ; (5) $V_{sub} = 35.5\mu$m/s, $\lambda = 245\mu$m.

REFERENCES

[1] Moffat J.R., Sefiane K. and Shanahan E.R., *J. Phys. Chem.*, **113** (2009) 8860-8866

[2] Hsueh C., Moraila Martinez C.L., Doumenc F. Rodriguez-Valverde M.A. and Guerrier B., *Chem. Eng. Process.*, **68** (2013) 64-68

[3] Adachi E., Dimitrov A.S. and Nagayama K., *Langmuir*, **11** (1995) 1057-1060

[4] Xu J.,Xia J.,Hong S.W., Lin Z., Qiu F. and Yang Y., *Phys. Rev. Lett.*, **96** (2006) 066104

[5] Abkarian M., Nunes J. and Stone H.A., *J. Am. Chem. Soc.*, **126** (2004) 5978-5979.

[6] Ghosh M., Fan F. and Stebe K.J., *Langmuir*, **23** (2007) 2180-2183.

[7] Bodiguel H., Doumenc F. and Guerrier B., *Langmuir*, **26** (2010) 10758-10763.

[8] Bodiguel H., Doumenc F. and Guerrier B., *Langmuir*, **27** (2011) 15352 (erratum).

[9] Rio E., Daerr A., Lequeux F. and Limat L., *Langmuir*, **22** (2006) 3186-3191.

[10] Hong S.W., Xia J., Byun M., Zou Q. and Lin Z., *Macromolecules*, **40** (2007) 2831-2836

[11] Le Berre M., Chen Y. and Baigl D., *Langmuir*, **25** (2009) 2554-2557.

[12] Frastia L., Archer A. J. and Thiele U., *Soft Matter*, **8** (2012) 11363-11386.

[13] Warner M. R. E., Craster R. V. and Matar O. K., *J. Colloid Interface Sci.*, **267** (2003) 92-110.

[14] Frastia L., Archer A. J. and Thiele U., *Phys. Rev. Lett.*, **106** (2011) 077801.

[15] Craster R. V., Matar O. K. and Sefiane K., *Langmuir*, **25** (2009) 3601.

[16] Köpf M. H., Gurevich S. V., Friedrich R. and Chi L., *Langmuir*, **26** (2010) 10444-10447.

[17] Doumenc F. and Guerrier B., *Langmuir*, **26** (2010) 13959-13967.

[18] Oron A., Davis S.H. and Bankoff S.G., *Rev. Mod. Phys.*, **69** (1997) 931-980.

[19] Flory P.J., *Principles of polymer chemistry* (Cornell University Press, Ithaca, NY) 1953

[20] Doumenc F., Guerrier B. and Allain C., *J. Chem. Eng. Data*, **50** (2005) 983-988.

[21] Dimitrov A.S. and Nagayama K., *Langmuir*, **12** (1996) 1303-1311.

[22] Jing G, Bodiguel H., Doumenc F. and Guerrier B., *Langmuir*, **26** (2010) 2288-2293.

[23] Berteloot G., Pham C.-T., Daerr A., Lequeux F. and Limat L., *Europhys. lett.*, **83** (2008) 14003.

[24] Carles P. and Cazabat A.M., *MRS Proceedings*, **248** (1991) 519.

[25] Poulard C. and Damman P., *Europhys. lett.*, **80** (2007) 64001.

[26] Li L., Köpf M. H., Gurevich S. V., Friedrich R. and Chi L., *Small*, **8** (2012) 488-503.

[27] Köpf M. H., Gurevich S. V., Friedrich R. and Thiele U., *New J. Phys.*, **14** (2012) 023016.

[28] Cazabat A.M., Heslot F., Troian S.M. and Carles P., *Nature*, **346** (1990) 824-826.